



HAL
open science

Influence of turbulent natural convection on heat transfer in shallow caves

B. Qaddah, Laurent Soucasse, Frédéric Doumenc, Sophie Mergui, Philippe Riviere, Anouar Soufiani

► **To cite this version:**

B. Qaddah, Laurent Soucasse, Frédéric Doumenc, Sophie Mergui, Philippe Riviere, et al.. Influence of turbulent natural convection on heat transfer in shallow caves. *International Journal of Thermal Sciences*, 2022, 177, pp.107524. 10.1016/j.ijthermalsci.2022.107524 . hal-03606905

HAL Id: hal-03606905

<https://hal.science/hal-03606905>

Submitted on 12 Mar 2022

HAL is a multi-disciplinary open access archive for the deposit and dissemination of scientific research documents, whether they are published or not. The documents may come from teaching and research institutions in France or abroad, or from public or private research centers.

L'archive ouverte pluridisciplinaire **HAL**, est destinée au dépôt et à la diffusion de documents scientifiques de niveau recherche, publiés ou non, émanant des établissements d'enseignement et de recherche français ou étrangers, des laboratoires publics ou privés.

Highlights

Influence of turbulent natural convection on heat transfer in shallow caves

B. Qaddah, L. Soucasse, F. Doumenc, S. Mergui, Ph. Rivière, A. Soufiani

- Large-eddy simulations of natural convection in a confined shallow cave are performed using wall temperature distributions representative of different times of the year.
- We propose a general approach to predict heat transfer in a shallow confined cave, and analyse the role of convection and radiation.
- Two flow regimes are found depending on the direction of the mean vertical temperature gradient.
- Heat transfer coefficients are calculated from the simulations and the use of the Newton's law to predict the heat flux at cave walls is discussed.

Influence of turbulent natural convection on heat transfer in shallow caves

B. Qaddah^a, L. Soucasse^a, F. Doumenec^{b,c}, S. Mergui^{b,c}, Ph. Rivière^a, A. Soufiani^a

^a*Laboratoire EM2C, CNRS, CentraleSupélec, Université Paris-Saclay, 8-10 rue Joliot Curie, 91192 Gif-sur-Yvette, France*

^b*Université Paris-Saclay, CNRS, FAST, 91405, Orsay, France*

^c*Sorbonne Université, UFR 919, 4 place Jussieu, F-75252, Paris Cedex 05, France*

Abstract

We aim at analyzing in detail the different heat transfer mechanisms involved in a confined shallow cave embedded in a rock massif submitted to seasonal variations of the ground temperature. Heat conduction in the rock massif, radiative heat transfer between cave walls, and turbulent natural convection inside the cave are considered. The natural convection problem is solved by large-eddy simulations (LES) using a Chebyshev pseudo-spectral method associated with a spectral vanishing viscosity (SVV) model. The thermal boundary conditions applied to the cave walls are obtained from a large-scale model that takes into account heat conduction in the rock massif and radiative fluxes between cave walls. This approach allows us to characterize the relative strength of convective and radiative fluxes and to identify the regions of the cavity and times of the year of intense heat transfer. We identified two different flow regimes: (i) a one-cell flow regime associated with strong convection, high turbulence level and unstable mean vertical temperature gradient, (ii) a multiple-cell flow regime associated with weak convection, low turbulence level and stable mean vertical temperature gradient. The use of the Newton's law to describe convection heat fluxes at the cavity walls is discussed.

Keywords: Shallow caves, Turbulent natural convection, Heat transfer, Large-eddy simulation, Spectral vanishing viscosity

Email address: qaddah.baraa@centralesupelec.fr (B. Qaddah)

1. Introduction

Karsts are landscapes formed from the dissolution of soluble rocks, for instance limestone or gypsum [1]. The chemical erosion due to rainwater results in the formation of an extensive network of caves. Heat transfer in karstic massifs is at the core of many issues, as diverse as paleoclimate reconstruction from speleothem analysis [2], consequences of tunneling on the environment [3], evolution of subterranean flora and fauna [4], or conservation of parietal prehistoric paintings [5, 6]. However, assessing temperature fields and heat fluxes in karstic massifs is complicated by the coupling between several heat transfer mechanisms, as heat conduction in the rock and convection due to air and water circulation in caves [7], possibly with latent heat exchanges due to condensation/evaporation or even ice formation [8].

In this work, we focus on caves located at a shallow depth, typically on the order of 10 meters. This configuration corresponds to that of many painted caves in France (Lascaux [9], Marsoulas and Pech Merle [10]) and throughout the world (Altamira in Spain [5], Takamatsuzuka Tumulus in Japan [11]). The exceptional state of conservation of parietal paintings (some of which are more than 10,000 years old) is mainly due to the high stability of cave microclimate. Painting damages can occur when this microclimate is disturbed. Human visits may result in significant climate perturbations in a number of different ways, directly (increase in temperature, humidity and CO₂ concentration, resulting in enhanced condensation and corrosion on cave walls [12]) or indirectly (need for an artificial ventilation, modification of cave entrance to allow visits as in Lascaux [9] or Marsoulas [10]). In some cases, the cessation or the limitation of visits is not enough to restore favourable conditions for conservation, and remediation may be necessary (e.g., thermal insulation of the Takamatsuzuka Tumulus [11]). A deep understanding of the physical mechanisms driving heat transfer inside a cave and between a cave and its external environment is therefore necessary to improve the conservation of painting cave heritage.

The damping of the external temperature fluctuations by the rock massif surrounding a confined cave is the main reason for its high thermal stability (by confined cave, we mean a cave for which mass transfer with the external environment can be neglected). Quindos and coworkers [13, 5] measured the amplitude and phase shift of the annual temperature variations at the roofs of Altamira Cave, at different locations of varying depth (from 3.5 m to 17.5 m), and found a good agreement with the prediction of the periodic

38 1D conduction model. In the range of depth from a few meters to approxi-
39 mately 10 m, daily temperature fluctuations can be considered as completely
40 damped, while annual temperature fluctuations are still perceptible.

41 Due to complex cave geometry and depth variations all along the cave,
42 temperature levels inside the cave (i.e., wall and air temperatures) vary not
43 only in time, but also in space. Quindos *et al* [5] found that the amplitude and
44 phase shift at the floors of Altamira Cave were close to the values measured at
45 the roofs, which they attributed to radiative heat transfer between cave walls.
46 Guerrier *et al* [14] confirmed by numerical simulations the significant role of
47 thermal radiation in the homogenization of the temperature field inside a
48 confined cave. However, spatial temperature variations are not strictly zero.
49 For instance, temperature differences on the order of 0.1 K were commonly
50 measured between the walls of the Hall of Bulls in Lascaux Cave [15]. This is
51 enough to trigger significant natural convection flow. Indeed, assuming a cave
52 height of 5 m, the Rayleigh number comparing buoyancy and diffusion is on
53 the order of 10^9 , denoting possible turbulent flow at least in some parts of the
54 cave [16, 17]. In addition, relative humidity is often close to 100 % in confined
55 caves [5, 10], due to the presence of thin liquid films of percolating water on
56 the walls and weak ventilation. Therefore, small temperature variations can
57 induce condensation/evaporation at the walls, so that latent heat exchange
58 must be considered. Due to seasonal variations of water intake [18], air
59 humidity [5] and wall temperatures, condensation/evaporation mass fluxes
60 are expected to vary in time. In conclusion, a minimal model for a shallow
61 confined cave must consider heat conduction in the rock massif, radiative heat
62 transfer between cave walls, and turbulent natural convection inside the cave.
63 In addition, the significance of latent heat exchanges due to condensation and
64 evaporation must be assessed.

65 The numerical investigation of cave climate is clearly restricted by the
66 computational effort required to simulate 3D turbulent natural convection.
67 If the gas is assumed to be transparent, radiative transfer between opaque
68 walls can be efficiently computed using view factors. A simple approach
69 to account for convection without solving the Navier–Stokes equations is to
70 estimate the wall convective heat fluxes from the Newton’s law [11, 14]. A
71 considerable drawback of this method is the need for empirical correlations to
72 estimate heat transfer coefficients, whereas available correlations refer to cav-
73 ities of simple geometry with uniform thermal boundary conditions on each
74 wall [19]. These conditions are far from being fulfilled in natural cavities,
75 making the estimation of heat transfer coefficients inaccurate. In contrast,

76 some authors rely on Computational Fluid Dynamics (CFD) to get better
77 insights on convection in caves [6, 20]. Assuming laminar flow, Lacanette *et*
78 *al.* [20] developed specific numerical methods to solve for air velocity, temper-
79 ature and moisture fields in Lascaux cave. Two sets of prescribed boundary
80 conditions, representative of climate conditions in 1980 and 1999, were con-
81 sidered.

82 In this article, we aim at analyzing in detail the different mechanisms
83 involved in heat transfer in a confined shallow cave embedded in a rock
84 massif. Ideally, we should consider a problem where heat conduction in
85 the rock, radiative transfer between the cave walls, and turbulent natural
86 convection inside the cave are fully coupled, and solve a 1-year periodic
87 regime. However, a one-year CFD simulation is not practicable with current
88 computational resources. We thus proceed as follows. We first define a
89 large-scale model, including heat conduction in the rock massif and radiative
90 heat transfer between the cave walls, but neglecting convection inside the
91 cave. Solving the periodic regime provides temperature fields in the rock
92 massif (including the cave walls) all along the year. Then we select six wall
93 temperature fields (spaced two months apart) representative of the different
94 thermal states encountered in the cave over the year. These temperature
95 fields are used as boundary conditions to solve the natural convection problem
96 inside the cave by a detailed flow simulation.

97 The thermal conductive fluxes in the air at the cave walls (i.e., the ther-
98 mal “convective” fluxes) obtained from the detailed flow simulation are then
99 compared with the radiative fluxes predicted by the large-scale model. Two
100 cases may arise:

- 101 • the thermal conductive fluxes at the cave walls are much smaller than
102 the radiative fluxes, and disregarding convection in the large-scale
103 model was a valid assumption. The temperature and velocity fields
104 inside the cave are known from the detailed flow simulation. If hu-
105 mid air was considered, the vapor concentration field in the cave and
106 evaporation/condensation mass fluxes at the cave walls would also be
107 known.

- 108 • the thermal conductive fluxes at the cave walls are larger than the ra-
109 diative fluxes. In this case, natural convection significantly contributes
110 to the uniformization of the wall temperature fields. Since this effect
111 was not taken into account in the large-scale model, the intensity of
112 the natural convection flow is likely overestimated. Conduction fluxes

113 at the cave walls can thus be regarded as higher bounds of the actual
114 ones, which is still a useful information. This approach also provides
115 higher bounds of evaporation/condensation mass fluxes when humid
116 air is considered.

117 For the sake of simplicity, we consider a parallelepiped cavity, but more
118 complex geometries could be treated with the same global approach. As a
119 first step, we only consider in this article the limiting case of dry air (latent
120 heat exchanges are thus disregarded). The large-scale model is solved using
121 the finite element method. The turbulent convection flow inside the cave
122 is obtained from large-eddy simulations (LES) performed with a Chebyshev
123 pseudo-spectral method associated with a spectral vanishing viscosity (SVV)
124 model [21].

125 The paper is organised as follows. We first describe the large-scale model
126 used to obtain temperature fields at cave walls (Sec. 2). Then we present
127 the LES model used for the simulation of the natural convection flow inside
128 the cave, and its numerical validation (Sec. 3). We discuss in section 4 the
129 different flow regimes observed depending on the season, as well as turbulent
130 statistics. We analyse in section 5 the heat flux distributions at the walls.
131 Conducto-convective fluxes are compared with radiative fluxes. Concluding
132 remarks are presented in section 6.

133 2. Large-scale model

134 2.1. Governing equations

135 The large-scale model is a 3D extension of the 2D model defined by
136 Guerrier *et al* [14]. We consider the confined parallelepiped cavity embedded
137 in the rock massif displayed in Fig. 1a. The ground surface is inclined at 10°
138 from the horizontal direction. The left upper edge of the cavity is located at
139 a depth of 7.3 m. The cave dimensions are the height $L_X = 5.3$ m, the width
140 $L_Y = 7$ m and the length $L_Z = 17$ m (see Fig. 2a), which roughly reflect
141 the size of the Hall of Bulls in Lascaux Cave. The gravity acceleration field
142 corresponds to $\mathbf{g} = -g\mathbf{X}$.

143 Conductive heat transfer is assumed in the rock massif:

$$\frac{\partial T_r}{\partial t} = \alpha_r \nabla^2 T_r, \quad (1)$$

144 where T_r is the rock temperature, t the time and $\alpha_r = 8 \times 10^{-7} \text{ m}^2 \cdot \text{s}^{-1}$ the
145 limestone diffusivity [14]. A time-periodic Dirichlet condition is imposed at

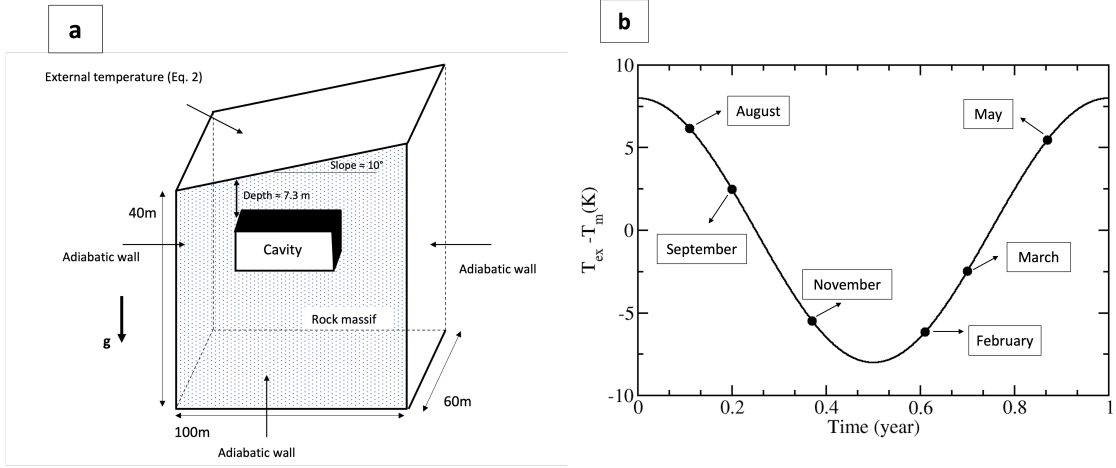


Figure 1: a) Geometry setup for the large-scale model (not at scale). b) Time evolution over a one-year period of the external temperature fluctuation $T_{ex}(t) - T_m$ applied at the upper surface of the massif. The six filled circles correspond to the six months that we investigate (see the corresponding times in Tab. 1).

146 the upper surface of the rock massif (see Fig. 1a):

$$T_{ex}(t) = T_m + A \cos\left(2\pi \frac{t}{\tau}\right), \quad (2)$$

147 where T_{ex} is the external ambient temperature, $\tau = 1$ year is the period,
 148 $T_m = 12^\circ\text{C}$ is the annual average external temperature and $A = 8^\circ\text{C}$ is the
 149 amplitude of the temperature variations (these values of T_m and A are typ-
 150 ical of the climate conditions in south-west of France). The time evolution
 151 of T_{ex} is displayed in Fig. 1b, where the six months that will be investi-
 152 gated using the LES model are highlighted. As we only consider the periodic
 153 regime, we arbitrarily assume that the initial time corresponds to the hottest
 154 temperature of the year that takes place in July.

155 The lateral and bottom sides of the massif are adiabatic. With the
 156 approximation of black walls (the emissivity of limestone is 0.96 [19], i.e.,
 157 close to 1), and disregarding convection as explained in the introduction, the
 158 boundary condition at cave walls reads

$$-\lambda_r \nabla T_r \cdot \mathbf{n} = \sigma T^4 - \int_{\Omega \cdot \mathbf{n} < 0} I(\Omega) |\Omega \cdot \mathbf{n}| d\Omega, \quad (3)$$

159 where $\lambda_r = 1.656 \text{ W}\cdot\text{m}^{-1}\cdot\text{K}^{-1}$ is the rock thermal conductivity [14], \mathbf{n} is the
 160 normal vector pointing to the cavity, σ is the Stefan-Boltzmann constant

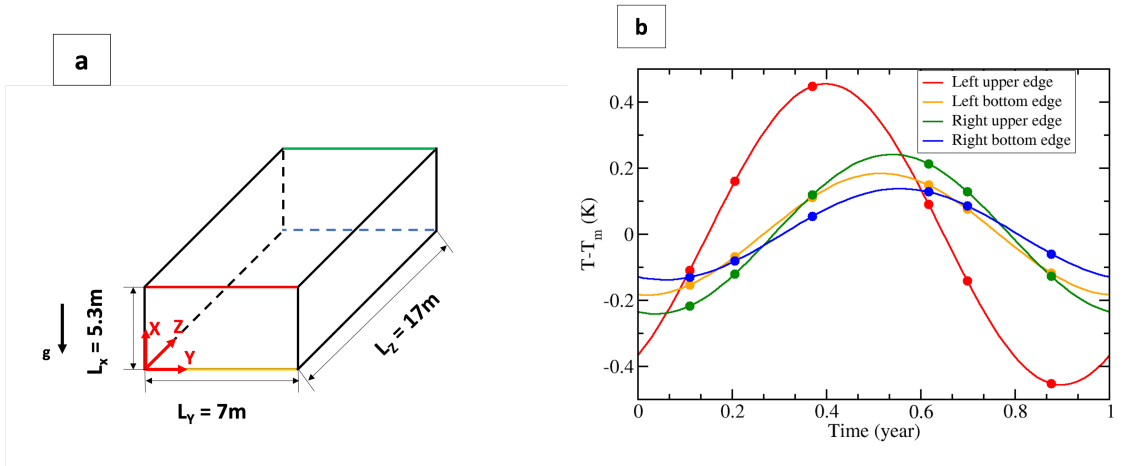


Figure 2: a) Geometry setup of the cavity. b) Time evolution of the temperature fluctuations $T(t) - T_m$ averaged on four edges of the cave. Red, yellow, green and blue lines correspond to the left upper ($Z = 0$ and $X = L_X$), left bottom ($Z = 0$ and $X = 0$), right upper ($Z = L_Z$ and $X = L_X$) and right bottom ($Z = L_Z$ and $X = 0$) edges, respectively (the colors of the edges in Fig. 2a, and of the curves in Fig. 2b correspond to each other). The six months that we investigate are marked with filled circles.

161 and $I(\boldsymbol{\Omega})$ is the radiative intensity (integrated over the infrared spectrum) in
 162 direction $\boldsymbol{\Omega}$. The air is supposed to be transparent. Therefore, $I(\boldsymbol{\Omega})$ depends
 163 on wall temperatures, and does not depend on the temperature field of the
 164 gas phase.

165 The model defined by Eqs.(1-3) is solved using the commercial software
 166 Comsol Multiphysics (Galerkin method, time discretization based on implicit
 167 backward differentiation formulas). The computational domain is discretized
 168 with a total of approximately 530,000 quadratic Lagrangian tetrahedron el-
 169 ements. The view factors related to surface elements on cave walls are cal-
 170 culated using the hemicube method [22].

171 2.2. Results from the large-scale model

172 We discuss the six wall temperature fields resulting from the simulation
 173 of the large-scale model, at months of the year indicated in Fig. 1b. The wall
 174 temperature fields in February, March and May are displayed in Fig. 3. The
 175 wall temperature fields for the months of August, September and November
 176 (not shown) can be deduced by symmetry from those of February, March
 177 and May respectively, thanks to the yearly periodicity. Despite the simple

178 geometry of the cave, the wall temperature fields are rather complex. Be-
 179 cause of conductive damping in the rock and temperature uniformization by
 180 radiative transfer inside the cavity, temperature gradients are larger along
 181 the vault than along the floor, the latter being quasi-isothermal. The max-
 182 imum wall-temperature difference $\Delta T = T_{max} - T_{min}$ is reported in Tab. 1
 183 for each month: it is minimal in February/August (0.124 K) and maximal in
 184 May/November (0.492 K).

185 We can gain more insight by considering in Fig. 2b the time evolution
 186 of the temperature averaged on the four edges highlighted in Fig. 2a. The
 187 average temperature of the upper left edge, which is the closest to the ground
 188 surface, evolves with larger amplitude and different phase shift compared to
 189 that of the other edges, whose temperatures differ little from each other.
 190 More specifically, the phase shifts of the left upper edge (depth $d = 7.3$ m)
 191 and of the right upper edge (depth $d = 10.3$ m) are respectively 0.40 and
 192 0.53 year. This is close to the values 0.41 and 0.58 year predicted by a 1D
 193 semi-infinite model for which the phase shift is $d\sqrt{\tau/(4\pi\alpha_r)}$. The complexity
 194 of the wall temperature fields thus results from the small 10° slope between
 195 the ground and the horizontal plane (see Fig. 1a). Consequences on the flow
 196 structure will be analysed in Sec. 4 by using these wall temperature fields as
 197 thermal boundary conditions in the LES.

198 3. Large-eddy simulation model

199 3.1. Governing equations

200 The air filling the cavity is assumed to be dry, transparent and at at-
 201 mospheric pressure. Following the Boussinesq approximation, the physical
 202 properties of the fluid are assumed to remain constant, except in the buoy-
 203 ancy term of the momentum equation where the density is assumed to vary
 204 linearly with temperature. The natural convection flow induced in the cavity
 205 is therefore governed by the following dimensionless equations:

$$\nabla^* \cdot \mathbf{u}^* = 0, \quad (4)$$

$$\frac{\partial \mathbf{u}^*}{\partial t^*} + \mathbf{u}^* \cdot \nabla^* \mathbf{u}^* = -\nabla^* p^* + Pr T^* \mathbf{x}^* + \frac{Pr}{Ra^{0.5}} \nabla^{*2} \mathbf{u}^* \quad (5)$$

$$\frac{\partial T^*}{\partial t^*} + \mathbf{u}^* \cdot \nabla^* T^* = \frac{1}{Ra^{0.5}} \nabla^{*2} T^*, \quad (6)$$

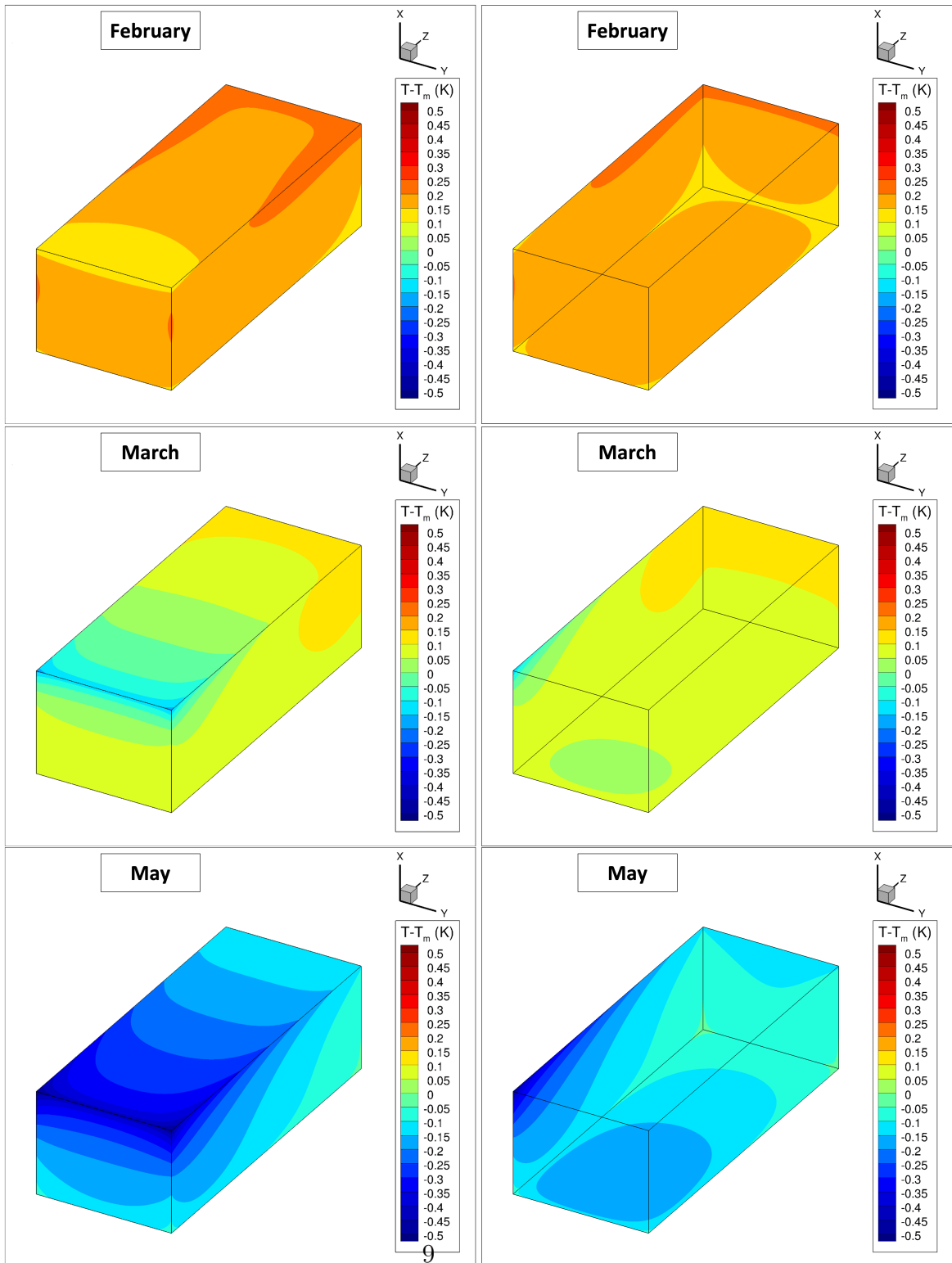


Figure 3: Wall temperature fields $T - T_m$ computed from the large-scale model for three months: February, March and May, from top to bottom. The left panels correspond to the upper ($X = L_X$), left ($Z = 0$) and front ($Y = L_Y$) cave walls. The right panels correspond to the bottom ($X = 0$), right ($Z = L_Z$) and back ($Y = 0$) cave walls.

206 where * denotes dimensionless variables and \mathbf{u} , p , T are respectively the
 207 velocity vector, the motion pressure and the temperature. Equations are
 208 made dimensionless using the reference height L_X , the reference time $t_{ref} =$
 209 $L_X^2/(\alpha Ra^{0.5})$, and the reference temperature scale ΔT . The reduced tem-
 210 perature thus reads $T^* = (T - T_0)/\Delta T$, where $T_0 = (T_{max} + T_{min})/2$ is
 211 the reference temperature. $Pr = \nu/\alpha = 0.712$, and $Ra = g\beta\Delta TL_X^3/(\alpha\nu)$
 212 are respectively the Prandtl number, and the Rayleigh number, where $\alpha =$
 213 $2.05 \times 10^{-5} \text{ m}^2.\text{s}^{-1}$ is the thermal diffusivity, $\nu = 1.46 \times 10^{-5} \text{ m}^2.\text{s}^{-1}$ is the
 214 kinematic viscosity and $\beta = T_0^{-1}$ is the thermal expansion coefficient.

215 Hydrodynamic and thermal boundary conditions at cave walls are zero
 216 velocity (no-slip) and one of the temperature fields provided by the large-
 217 scale model. Wall temperatures are assumed to be time-independent. This
 218 is justified by the large time scale associated with the time evolution of the
 219 wall temperature compared to the small characteristic time scale associated
 220 with the convection inside the cave. Indeed, the characteristic time scale of
 221 conduction in the rock for a depth equal to 7.3 m is about 2 years, which is of
 222 the same order as the period of 1 year characterizing the change of external
 223 boundary conditions, while the circulation time (or convection time), based
 224 on the computed velocities is of the order of a few minutes. The time required
 225 to reach statistically steady flows in the numerical simulations is of the order
 226 of 1 hour, which is also much smaller than one year.

227 One of the main outcome of the simulation is the distribution of the
 228 conductive flux at the walls, to be compared with the radiative flux from the
 229 large-scale model. The conductive flux through the walls in the gas phase
 230 reads

$$q_{con} = -\lambda \nabla T \cdot \mathbf{n}, \quad (7)$$

231 where $\lambda = 2.51 \times 10^{-2} \text{ W.m}^{-1}.\text{K}^{-1}$ is the air conductivity. The dimensionless
 232 counterpart of Eq. (7) is

$$Nu = -\nabla^* T^* \cdot \mathbf{n}, \quad (8)$$

233 where $Nu = q_{con} L_X / (\lambda \Delta T)$ is the Nusselt number at the walls.

234 The values of ΔT , T_0 and Ra for the six cases considered in the LES are
 235 listed in Tab. 1. Notice that similar values of Ra may correspond to different
 236 wall temperature fields resulting in different flow structures, as will be seen
 237 in section 4.

Time	Month	ΔT (K)	T_0 (K)	$Ra \times 10^{-9}$
0.11 τ	August	0.124	284.985	2.13
0.20 τ	September	0.312	285.165	5.35
0.37 τ	November	0.492	285.419	8.41
0.61 τ	February	0.124	285.315	2.13
0.70 τ	March	0.312	285.135	5.35
0.87 τ	May	0.492	284.881	8.43

Table 1: Maximum temperature difference ΔT , reference temperature T_0 and Rayleigh number Ra for the six wall temperature fields used as boundary conditions in the LES ($\tau = 1$ year).

238 3.2. Numerical methods

239 The large-eddy simulation (LES) approach is used in this study to save
240 computational time. Simulations are performed using a Chebyshev pseudo-
241 spectral method (detailed in Sec. 3.2.1), associated with a spectral vanishing
242 viscosity (SVV) method (detailed in Sec. 3.2.2) to model the effects of the
243 subgrid scales. In Sec. 3.3, we analyse the sensitivity of LES results to SVV
244 parameters and we compare LES results with Direct Numerical Simulation
245 (DNS) results in February, which corresponds to the smallest Rayleigh num-
246 ber investigated.

247 3.2.1. Chebyshev pseudo-spectral method

248 The flow governing equations are implemented in a spectral code close
249 to the one developed by Xin and Le Quéré [23], using a Chebyshev collocation
250 method for the three spatial dimensions. This type of spectral method
251 reaches a high spatial accuracy at a reasonable numerical cost. It assumes
252 that the required solution is represented on a finite basis of orthogonal func-
253 tions. The basis functions considered for the spatial discretization are the
254 Chebyshev polynomials, suitable for the development of non-periodic func-
255 tions. A projection method is used to ensure the pressure-flow coupling:
256 first, the momentum and heat equations are solved using the pressure field
257 from the previous time step; second, a pressure correction term is calculated
258 from a Poisson equation and the predicted velocity is corrected to force the
259 velocity divergence free condition. Time integration is performed using a
260 second-order semi-implicit temporal scheme, coupling a backward differenti-
261 ation (BDF2) scheme for the linear diffusion terms and an Adams Bashforth

262 extrapolation for the convective terms. Moreover, the computational domain
 263 is decomposed along the largest spatial direction (here the Z -horizontal di-
 264 rection) in order to perform parallel computations [24].

265 3.2.2. Spectral vanishing viscosity model

266 LES involves filtering the Navier-Stokes equations and solving only the
 267 large scales of a turbulent flow. The small scales of the flow are not solved but
 268 must be modeled. According to the filtering operation applied to the equa-
 269 tions (4)-(6), additional non-linear terms are generated with supplementary
 270 unknowns to be modeled by expressing them in terms of the filtered variables.
 271 For the momentum and heat transfer equations, the dimensionless supple-
 272 mentary terms are the subgrid scale stress tensor $\nabla^* \cdot \boldsymbol{\tau}_{LES}^* = \nabla^* \cdot (\overline{\mathbf{u}^* \mathbf{u}^*} -$
 273 $\overline{\mathbf{u}^*} \overline{\mathbf{u}^*})$ and the subgrid scale heat flux $\nabla^* \cdot \mathbf{q}_{LES}^* = \nabla^* \cdot (\overline{\mathbf{u}^* T^*} - \overline{\mathbf{u}^*} \overline{T^*})$ where
 274 \bar{a} denotes the spatial filtering operator of the variable a . These terms are
 275 usually modelled as diffusion terms [25].

276 Conventional LES models based on a subgrid viscosity are not suited
 277 for spectral methods, and we rely in this work on the Spectral Vanishing
 278 Viscosity (SVV) method [26, 27], which has been specially developed for
 279 them. It consists in the introduction of an artificial dissipation term to ensure
 280 the spectral convergence, i.e. dissipate the high modes of the Chebyshev
 281 polynomial development. The main feature of the SVV method is to maintain
 282 the spectral accuracy i.e. the exponential rate of convergence of the numerical
 283 solution [21]. This SVV method has been used for several applications such
 284 as turbulent channel flows [28], turbulent flows within rotating cavities [29]
 285 and turbulent wakes [30].

286 The SVV method is implemented in the form of a modified Laplacian
 287 operator combining the viscous and the SVV terms [21]. Hence, the modified
 288 Laplacian operator ∇_{SVV}^2 is given by

$$\nabla_{SVV}^2 = \nabla \cdot (1 + \nu^{-1} Q) \nabla, \quad (9)$$

289 where Q is the viscosity kernel and ν is the actual viscosity (in dimensionless
 290 form, equal to $PrRa^{-0.5}$ for momentum and $Ra^{-0.5}$ for energy equation).
 291 The viscosity kernel acts on each spatial direction independently. In spectral
 292 space, it is given for the i^{th} direction by

$$\hat{Q}_i(k) = \epsilon_i e^{\frac{-(k-N_i)^2}{(k-M_i)^2}}, \quad \text{if } k > M_i \quad (10)$$

$$\hat{Q}_i(k) = 0, \quad \text{if } k \leq M_i \quad (11)$$

294 where k is the Chebyshev polynomial order, ϵ_i is the viscosity amplitude, N_i
 295 is the number of collocation point in the i^{th} direction and $M_i \leq N_i$ is the cut-
 296 off spectral mode. ϵ_i and M_i are the control parameters of the SVV method.
 297 The numerical modeling reduces by either increasing M_i or decreasing ϵ_i . It
 298 is worth noting that the same SVV parameters are used in the momentum
 299 equation and in the energy equation. This would be similar to considering a
 300 subgrid Prandtl number equal to one in a conventional LES model based on
 301 subgrid viscosity and diffusivity.

302 3.3. Numerical validation

303 In order to study the accuracy of the SVV approach, we carry out a sen-
 304 sitivity analysis on the SVV parameters M_i and ϵ_i and on the mesh size. To
 305 this aim, we focus on the simulation of February (see Tab. 1), which corre-
 306 sponds to the smallest Rayleigh number investigated here (the less turbulent
 307 case) and for which DNS is practicable with current computational resources.

308 In a first step, we set the mesh size to $N_X \times N_Y \times (N_Z \times N_p) = 160 \times 160 \times$
 309 (20×32) (LES₁₆₀ mesh), where $N_{X/Y/Z}$ is the number of collocation points
 310 in directions $X/Y/Z$ in each subdomain and N_p is the number of processors,
 311 and we vary M_i and ϵ_i as described in Tab. 2. The results are presented
 312 in terms of time-averaged variables over a dimensionless time period of 100.
 313 The time-averaged fluxes through each of the six walls of the cavity are
 314 computed at each time step. The flow field is assumed to be statistically
 315 steady when the sum of these six fluxes is less than 1% of the maximum one.
 316 In Tab. 2, we calculate for each set of SVV parameters the volume-averaged
 317 temperature ($\langle T^* \rangle$), the volume-averaged kinetic energy of the mean flow
 318 ($k_{kin}^* = \langle u_i^* \rangle \langle u_i^* \rangle / 2$), the volume-averaged turbulent kinetic energy ($k_{tur}^* =$
 319 $\langle u_i^{*'} u_i^{*'} \rangle / 2$), and the Nusselt number ($Nu = -\nabla \langle T^* \rangle \cdot \mathbf{n}_{int}$) averaged over
 320 the upper ($X^*=1$), left ($Z^*=0$), and side ($Y^*=0$) walls separately ($\langle a \rangle$ and
 321 a' denote the time average and the fluctuation of a respectively). There is
 322 no influence of the SVV parameters on the average wall heat flux and the
 323 volume-averaged temperature in the system (the change is less than 1%). In
 324 addition, the SVV parameters have little effects on the kinetic energy of the
 325 mean flow (less than 3%) but significant effects (up to 10%) on the turbulent
 326 kinetic energy. Therefore, varying the SVV parameters has little influence on
 327 the time averaged fields as previously found in the application of turbulent
 328 wakes by Pasquetti [21].

329 In a second step, we fix the SVV parameters to $M_i = 3N_i/4$ and $\epsilon_i =$
 330 $1/(4N_i)$ and consider two LES meshes: $160 \times 160 \times (20 \times 32)$ (LES₁₆₀) and

SVV parameters	$\langle T^* \rangle \times 10^2$	$k_{kin}^* \times 10^4$	$k_{tur}^* \times 10^4$	$Nu_{up, X^*=1}$	$Nu_{left, Z^*=0}$	$Nu_{sides, Y^*=0}$
$M = N/2, \epsilon = 1/2N$	5.370	2.865	2.368	-16.385	6.046	7.192
$M = 2N/3, \epsilon = 1/3N$	5.367	2.889	2.274	-16.351	6.049	7.196
$M = 3N/4, \epsilon = 1/4N$	5.350	2.803	2.547	-16.385	5.979	7.219
$M = 4N/5, \epsilon = 1/5N$	5.341	2.880	2.504	-16.431	5.978	7.219

Table 2: Sensitivity to the SVV parameters of the volume-averaged temperature, the volume-averaged kinetic energy of mean flow, the volume-averaged turbulent kinetic energy and the wall-averaged Nusselt number for February.

331 $240 \times 240 \times (20 \times 32)$ (LES₂₄₀). Results are compared with those of a DNS
332 (no model or $M_i = N_i$ and $\epsilon_i = 0$) with a mesh of $320 \times 410 \times (32 \times 32)$ points.
333 The time required to perform the simulation for the dimensionless time $\Delta t^* =$
334 1000 with the DNS approach using the available resources is approximately
335 128000 hours. With the LES approach using LES₁₆₀ and LES₂₄₀ meshes, the
336 time decreases to 24576 hours and 55360 hours, respectively. In Tab. 3, the
337 same averaged variables described in Tab. 2 are recalculated for each case.
338 The results obtained with the LES₂₄₀ mesh are in good agreement with the
339 DNS (differences below 10%), while results obtained with the LES₁₆₀ mesh
340 show significant discrepancies with the DNS (up to 20%).

Case	$\langle T^* \rangle \times 10^2$	$k_{kin}^* \times 10^4$	$k_{tur}^* \times 10^4$	$Nu_{up, X^*=1}$	$Nu_{left, Z^*=0}$	$Nu_{sides, Y^*=0}$
DNS	5.760	2.540	2.710	-14.755	4.968	6.825
LES ₂₄₀	5.610	2.638	2.998	-15.605	5.381	6.961
LES ₁₆₀	5.350	2.803	2.547	-16.385	5.979	7.219

Table 3: Comparison between LES and DNS methods in terms of the volume-averaged temperature, the volume-averaged kinetic energy of mean flow, the volume-averaged turbulent kinetic energy and the average wall Nusselt number for February.

341 In order to get further insights on the accuracy of the SVV-LES model,
342 we compare LES₂₄₀ results and DNS results for the local distribution of key
343 quantities such as the Nusselt number and the turbulent kinetic energy. In
344 Fig. 4,a and b, we present the evolution of the Nusselt number along a hori-
345 zontal line at the upper wall ($X^* = 1, Y^* = 0.6604$) and along a vertical line
346 at the left wall ($Y^* = 0.6604, Z^* = 0$), respectively. The LES₂₄₀ mesh pro-
347 vides satisfactory results compared to the DNS with a small overestimation at

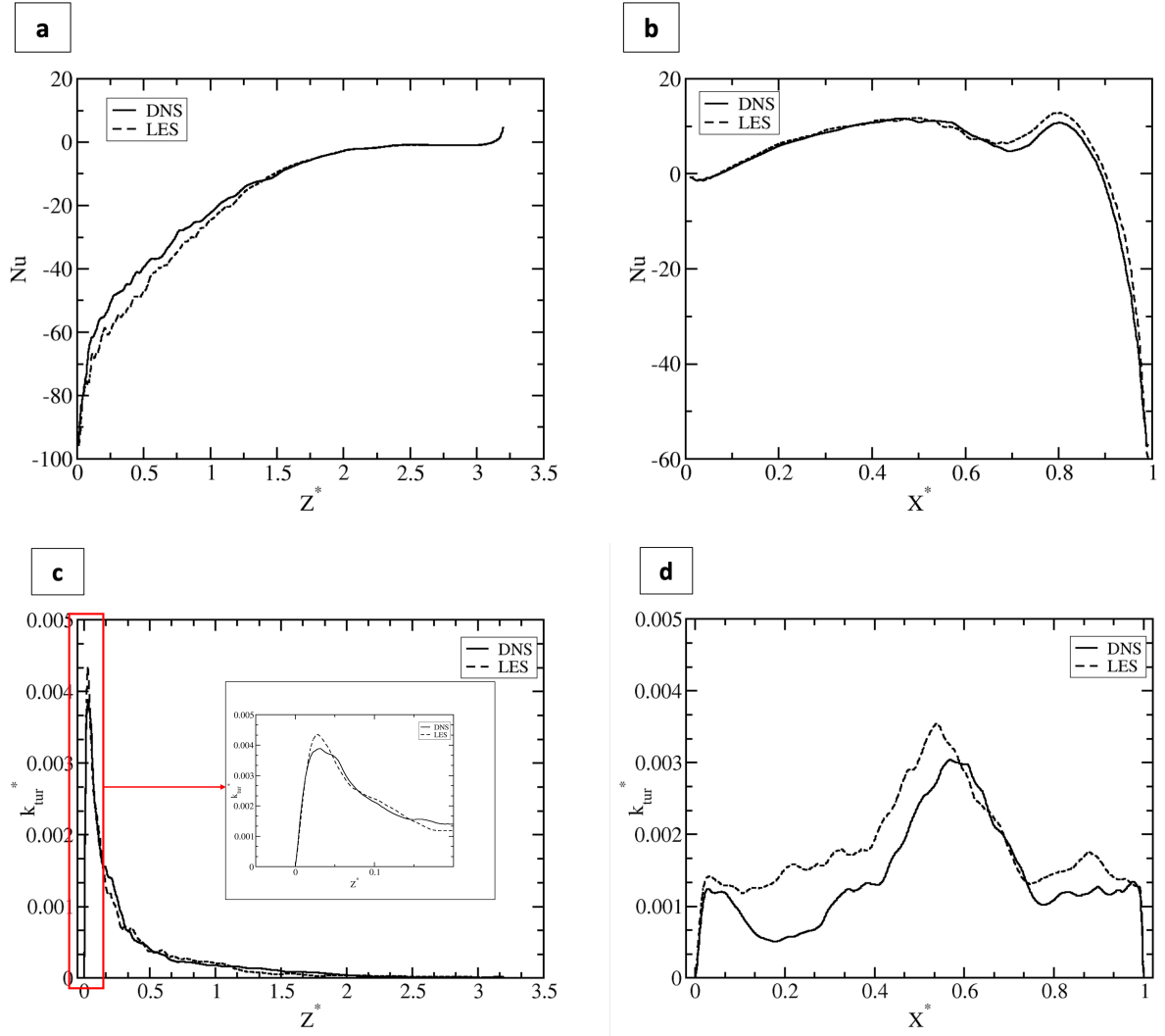


Figure 4: Nusselt number along the horizontal line $X^* = 1, Y^* = 0.6604$ (a) and the vertical line $Y^* = 0.6604, Z^* = 0$ (b) and turbulent kinetic energy along the horizontal line $X^* = 0.6, Y^* = 0.6604$ (c) and the vertical line $Y^* = 0.6604$ and $Z^* = 0.05$ (d) for February. The straight and dashed lines correspond to the DNS and LES₂₄₀ results, respectively.

348 locations associated with significant turbulent fluctuations. In Fig. 4, c and
 349 d, we plotted the turbulent kinetic energy along a horizontal line ($X^* = 0.6$,
 350 $Y^* = 0.6604$) and along a vertical line ($Y^* = 0.6604$, $Z^* = 0.05$), where
 351 these turbulent fluctuations are significant. The agreement between LES₂₄₀
 352 and DNS is rather good within the vertical boundary layer (c) while discrep-
 353 ancies are more important near the bottom wall (d) with overpredictions
 354 of the turbulent kinetic energy up to a factor of 2. Consequently, the SVV
 355 method with the LES₂₄₀ mesh preserves the heat flux at the walls but tends
 356 to overpredict the turbulent kinetic energy.

357 Since the main objective of this paper is to determine the role of turbulent
 358 convection on the heat fluxes at the cave walls and in order to save compu-
 359 tational time, we use the LES₂₄₀ mesh (CPU time savings of approximately
 360 44% compared to DNS) and SVV parameters $M_i = 3N_i/4$ and $\epsilon_i = 1/(4N_i)$
 361 for the simulation of all cases of Tab. 1.

362 4. Flow field analysis

363 4.1. One-cell and multiple-cell convection patterns

364 Figure 5 shows the streamlines of the mean airflow colored by the kinetic
 365 energy for each month studied, in the vertical Y mid-plane (the mean flow and
 366 mean temperature fields are mostly bidimensional thanks to the symmetry
 367 of the equations and boundary conditions with respect to the Y mid-plane).
 368 For all cases ascending or descending flows develop along the left and right
 369 vertical walls. They are connected through horizontal flows along the floor
 370 and the ceiling, giving rise to a primary rotating circulation in the cavity.
 371 However, we can define two distinct flow regimes depending on the period
 372 of the year: a one-cell regime in March, May and August (left panels in
 373 Fig. 5) characterized by a single large-scale circulation which extends over
 374 the entire cavity, and a multiple-cell regime in September, November and
 375 February (right panels in Fig. 5) for which the primary rotating flow near
 376 the walls is associated with more complex flow patterns within the core.

377 The different patterns can be schematically classified according to (i)
 378 the direction of rotation of the primary circulation along the walls, (ii) the
 379 number of cells in the bulk of the cavity. We are going to show that this
 380 classification results from the relative temperatures of the four edges men-
 381 tioned in Sec. 2.1, as illustrated in Fig. 6 where rather cold edges are marked
 382 in blue and rather hot in red. Indeed, it can be seen in Fig. 2b, that for each
 383 month there is one edge that is significantly hotter or colder than the three

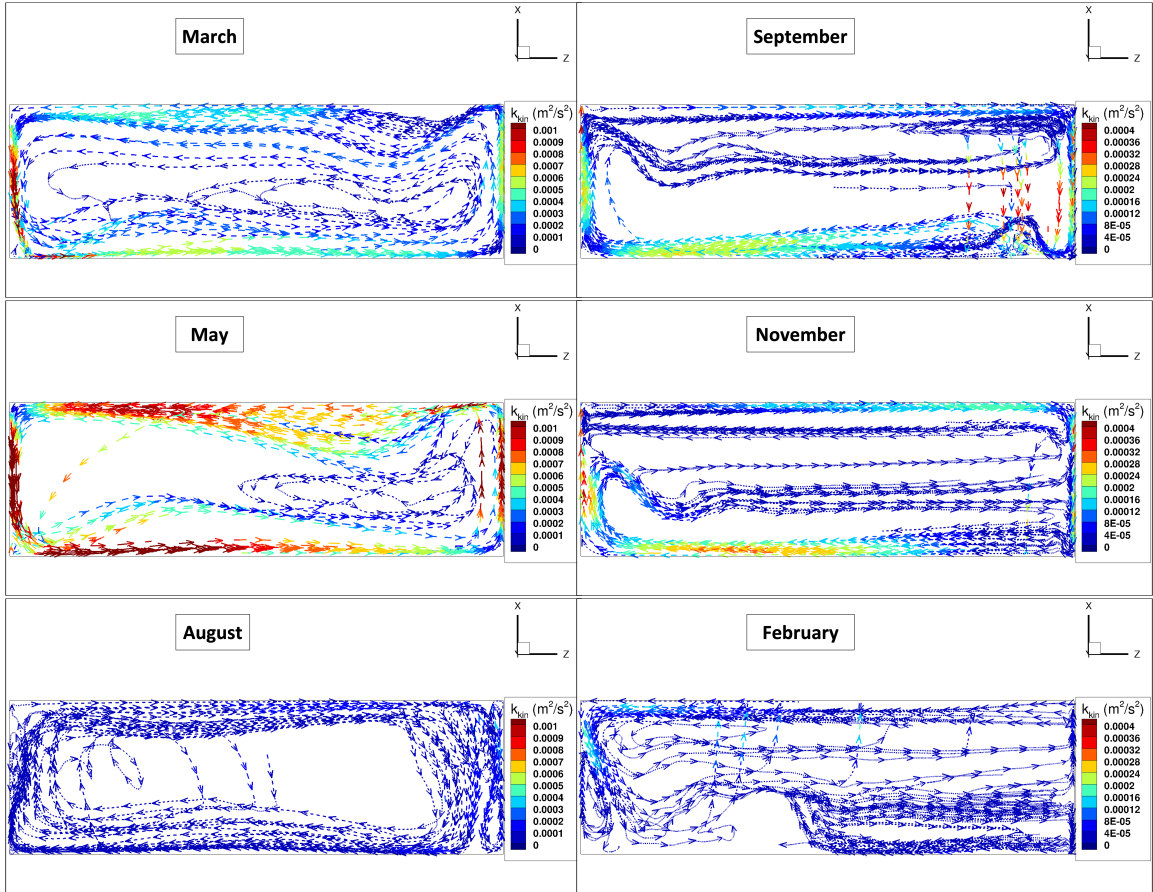


Figure 5: Flow streamlines colored by the kinetic energy of the mean flow. Streamlines are drawn from the Y mid-plane and then projected onto the Y mid-plane when they deviate from it.

384 others, which are almost at the same temperature. The direction of rotation
 385 of the primary circulation along the walls in the X - Z plane is determined by
 386 the sign of the horizontal temperature gradient along the Z axis. In March,
 387 May and February the right vertical wall is on average warmer than the left
 388 wall (the horizontal gradient is positive) giving rise to a counterclockwise
 389 rotation. Indeed, due to the buoyancy forces, the hot wall and the cold wall
 390 drive the air flow upward and downward, respectively. Conversely, the hori-
 391 zontal temperature gradient is negative in August, September and November
 392 resulting in a clockwise rotation. On the other hand, when the floor is on
 393 average warmer than the ceiling (March, May, August), the vertical temper-
 394 ature gradient is negative resulting in an unstable thermal stratification in
 395 the core and this corresponds to the one-cell regime. When the floor is on av-
 396 erage colder than the ceiling (September, November, February), the vertical
 397 temperature gradient is positive resulting in a stable thermal stratification
 398 and this corresponds to the multiple-cell regime. For example in November,
 399 three convection cells of weak intensity are observed. The air layer adjacent
 400 to the left wall is heated then rises but the outer part of this layer is cooled by
 401 the core then slows down and generates a horizontal current at mid-height.
 402 This current travels through the core to the right side then splits with a part
 403 incoming to the downward flow adjacent to the cold wall and another part,
 404 slightly warmer, moving upward thus creating recirculation cells.

405 Based on this simplified analysis of thermal boundary conditions, we can
 406 conclude that the global circulation along the vertical and horizontal walls
 407 is governed by the temperature variations between the vertical walls, i.e., by
 408 the horizontal temperature gradient, whereas the nature of the regime, one-
 409 cell or multiple-cell, is determined by the temperature variations between the
 410 horizontal walls, i.e., by the vertical temperature gradient.

411 In the following, we analyse the flow dynamics, the thermal features and
 412 the turbulence level of the one-cell and multiple-cell regimes. The volume-
 413 averaged kinetic energy of the mean flow, k_{kin} , the volume-averaged turbulent
 414 kinetic energy, k_{tur} , the maximum velocity, $\langle u \rangle_{max}$, and the volume-averaged
 415 standard deviation of the dimensionless mean temperature, $\sigma(\langle T^* \rangle)$, are given
 416 in Table 4 for each month. The one-cell regime is characterized by a strong
 417 mean flow compared to the multiple-cell regime, as indicated by relatively
 418 high k_{kin} and $\langle u \rangle_{max}$ values in May and March. In August, these quantities
 419 are comparable to those of September and November although the temper-
 420 ature difference ΔT is approximately 3 or 4 times smaller (see Tab. 1). The
 421 intense convection flow in the one-cell regime extends throughout the cavity

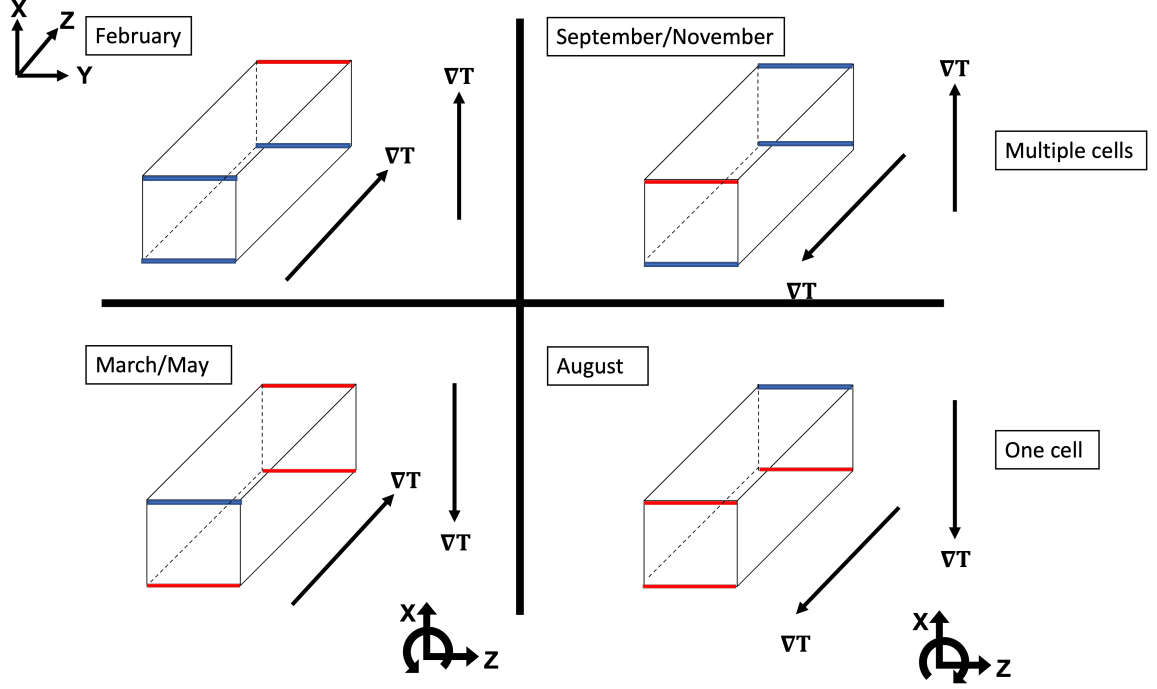


Figure 6: Simplified representation of thermal boundary conditions and associated flow regimes. Blue and red lines correspond to cold and hot edges, respectively.

Case	Regime	k_{kin} (m^2/s^2)	k_{tur} (m^2/s^2)	$\langle u \rangle_{max}$ (m/s)	$\sigma(\langle T^* \rangle)$
March	one-cell	1.6×10^{-4}	4.4×10^{-5}	0.076	0.018
May	one-cell	2.8×10^{-4}	9.3×10^{-5}	0.095	0.015
August	one-cell	3.5×10^{-5}	2.8×10^{-5}	0.045	0.011
September	multiple-cell	3.6×10^{-5}	8.8×10^{-6}	0.047	0.023
November	multiple-cell	3.1×10^{-5}	6.6×10^{-6}	0.050	0.044
February	multiple-cell	8.4×10^{-6}	1.0×10^{-5}	0.028	0.036

Table 4: Volume-averaged kinetic energy of the mean flow k_{kin} , volume-averaged turbulent kinetic energy k_{tur} , maximum velocity of the mean flow $\langle u \rangle_{max}$ and volume-averaged standard deviation of the dimensionless mean temperature $\sigma(\langle T^* \rangle)$ calculated for all months under study.

422 (see Fig. 5) leading to a strong mixing effect and thus the homogenisation
 423 of the temperature field. This gives rise to small values of $\sigma(\langle T^* \rangle)$ compared
 424 to the values related to the multiple-cell convection of weak intensity. To
 425 illustrate the analysis of the thermal feature, Fig. 7(top) displays the spatial
 426 distribution of the mean temperature in the Y mid-plane of the cavity. We
 427 focus on May (left panel) and November (right panel) as they correspond to
 428 the months with the greatest temperature amplitude (see Tab. 1) in the one-
 429 cell and multiple-cell regimes, respectively. In May, the temperature field is
 430 nearly isothermal thanks to the mixing effect of the large-scale convection
 431 cell. The temperature gradients are thus confined very close to the walls. By
 432 contrast, the temperature field in November shows significant temperature
 433 variations near the ceiling and a thermal stratification in the core related to
 434 the presence of the recirculation cells.

435 From the data reported in Table 4, we can see that the turbulent fluctu-
 436 ation level is higher in the one-cell regime than in the multiple-cell regime.
 437 It should be noted that, although the kinetic energy of the mean flow is very
 438 low in February, turbulent fluctuations are detected due to the presence of
 439 counter-rotating cells near the left wall (see Fig. 5). The spatial distribution
 440 of the turbulent kinetic energy is presented in Fig. 7 (bottom panels) for May
 441 and November. In May, significant turbulent fluctuations are noticeable in
 442 the lower left corner where the descending vertical boundary layer hits the
 443 floor and to a less extent in the upper right side. The asymmetry between
 444 the lower left and upper right corners is due to larger temperature gradients
 445 in the left part of the cavity than in the right part. In November, the tur-
 446 bulent kinetic energy is very small and turbulent fluctuations are detectable
 447 only in the left part of the cavity near the flow division and in the top right
 448 region where the downward flow in the cold boundary layer is sheared by the
 449 ascending recirculation flow (see Figure 5).

450 In order to visualize and compare the 3D turbulent structures in May
 451 and November, we make use of the Q -criterion $Q = [\Omega_{ij}\Omega_{ij} - S_{ij}S_{ij}]/2$
 452 [31], where $\Omega_{ij} = [\partial u_i/\partial x_j - \partial u_j/\partial x_i]/2$ is the vorticity tensor and $S_{ij} =$
 453 $[\partial u_i/\partial x_j + \partial u_j/\partial x_i]/2$ is the strain tensor. This criterion compares the rates
 454 of rotation and deformation. Turbulent structures correspond to positive val-
 455 ues of Q [32]. Figure 8 shows the Q -criterion colored by the kinetic energy
 456 of the mean flow for these two months, for a given instantaneous flow field
 457 in the asymptotic regime. Vortices almost spread everywhere in May, while
 458 they are restricted to regions near the left and right planes in November. It
 459 is interesting to note that the instantaneous flow is fully three-dimensional

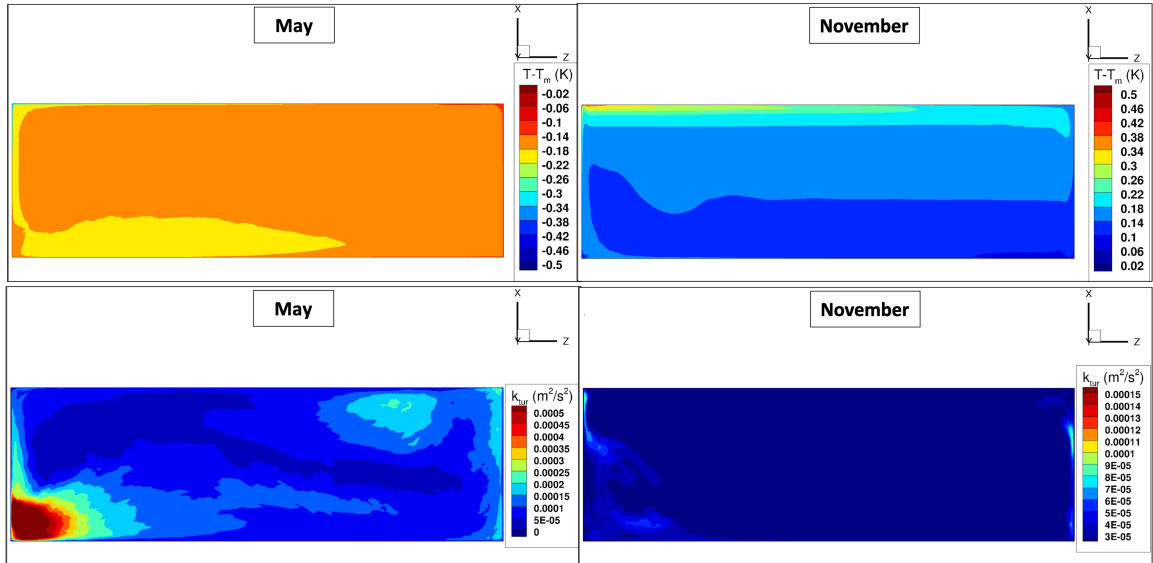


Figure 7: Mean temperature (top panels) and turbulent kinetic energy (bottom panels) fields in the Y mid-plane of the cavity for May and November.

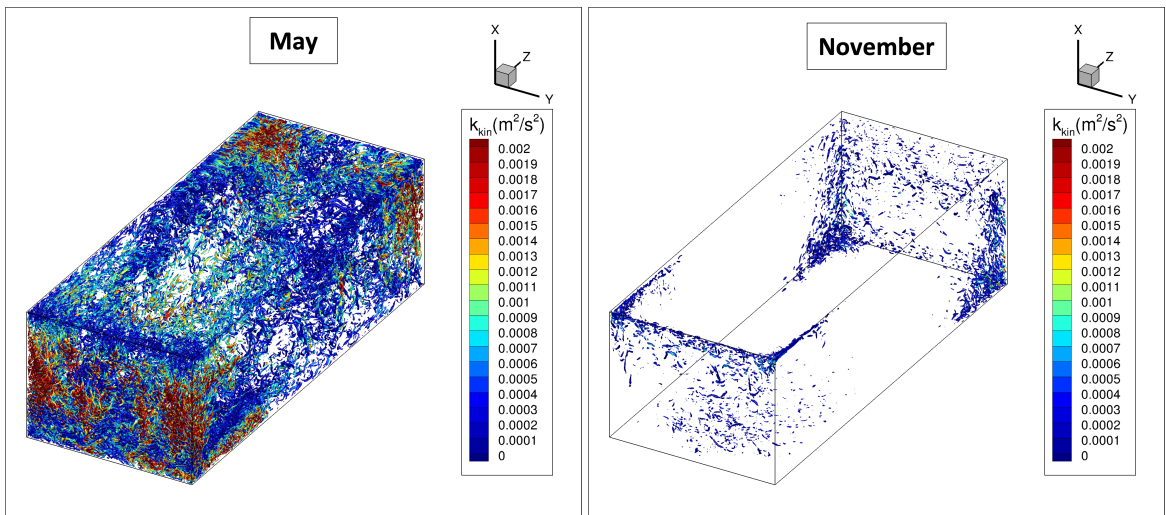


Figure 8: Isosurfaces of the Q -criterion colored by the kinetic energy of the mean flow for an instantaneous flow field for May and November. $Q = 1 \text{ s}^{-2}$ for all cases.

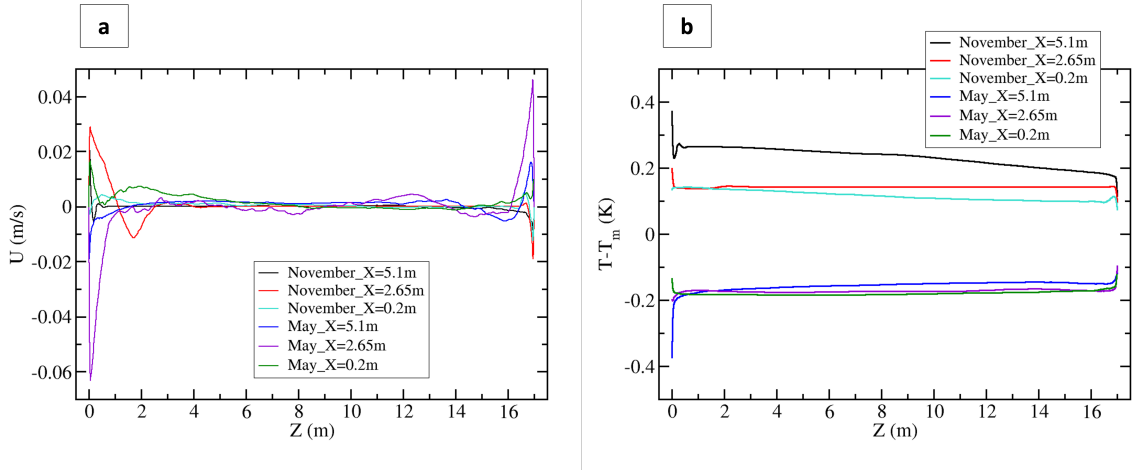


Figure 9: Horizontal profiles of the vertical velocity component U (a) and temperature (b) in the Y mid-plane for three different heights ($X = 0.2 \text{ m} \approx 0.04L_X$, $X = 2.65 \text{ m} = 0.5L_X$ and $X = 5.1 \text{ m} \approx 0.96L_X$). The vertical walls are located at $Z = 0$ and $Z = 17 \text{ m}$. May (one-cell regime) and November (multiple-cell regime) are presented.

460 for both months, though the main mean dynamics happen in the X - Z plane.

461 4.2. Near wall regions

462 To get a better insight into the flow structure in the near-wall region, we
 463 discuss in this section the temperature and velocity profiles along vertical or
 464 horizontal lines.

465 Fig. 9 presents horizontal profiles of the vertical velocity component U
 466 and the temperature in the Y mid-plane for three different heights ($X =$
 467 $0.2 \text{ m} \approx 0.04L_X$, $X = 2.65 \text{ m} = 0.5L_X$ and $X = 5.1 \text{ m} \approx 0.96L_X$), for May
 468 (one-cell regime) and November (multiple-cell regime). Velocity boundary
 469 layers are observed in Fig. 9 (a), ascending or descending according to the
 470 sign of the horizontal temperature gradients in the thermal boundary layers
 471 (see Fig. 9 (b)). It can be noted that in May, the horizontal temperature and
 472 velocity gradients change sign in the left bottom part ($X = 0.2 \text{ m}$, $Z \approx 0$)
 473 due to the presence of a small vortex in the corner (see Figure 5). The
 474 thickness of the velocity and thermal boundary are estimated as follows. The
 475 thickness of the velocity boundary layer, δ_u , is referred as the distance from
 476 the wall to a point where the velocity reaches an extremum. The thickness
 477 of the thermal boundary layer, δ_θ , is referred as the distance from the wall
 478 where the temperature reaches 90 % of its value in the core. We find that

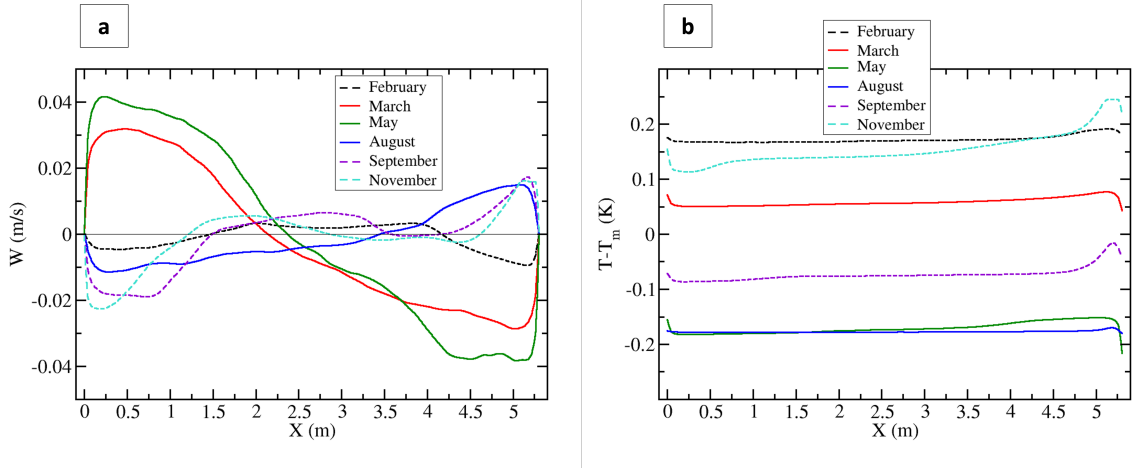


Figure 10: Vertical profiles of the horizontal velocity component W (a) and the temperature (b) along the vertical centerline ($Y = 0.5L_Y$, $Z = 0.5L_Z$) for the six months investigated. The horizontal walls are located at $X = 0$ and $X = 5.3$ m. The solid and dotted lines correspond to the one-cell and multiple-cell regime, respectively.

479 $\delta_u \sim \delta_\theta$ ranges from 4 cm to 8 cm, i.e., less than 0.5% of the cavity length
 480 ($L_Z = 17$ m).

481 As highlighted in subsection 4.1, Fig. 9 (b) shows that the core of the
 482 cavity is nearly isothermal in May whereas a stable vertical thermal strati-
 483 fication takes place in November, especially in the upper half of the cavity
 484 where a temperature difference of about 0.1 K is observed between the air at
 485 mid-height (red curve) and the air adjacent to the top wall (black curve).

486 Fig. 10 presents the horizontal velocity component W and the tempera-
 487 ture profiles along the vertical centerline ($Y = 0.5L_Y$, $Z = 0.5L_Z$), in the
 488 one-cell regime for March, May and August (solid lines) and in the multiple-
 489 cell regime for February, September and November (dashed lines). In the
 490 one-cell regime, Fig. 10 (a) exhibits the large-scale circulation extending over
 491 the entire height of the cavity, with a reverse direction of rotation for Au-
 492 gust compared to March and May. By contrast, the core is almost motion-
 493 less in the multiple-cell regime, with however small variations around zero
 494 that are the signature of the recirculations of low intensity. Temperature
 495 profiles (Fig. 10 (b)) confirm that the temperature gradients are confined
 496 in very thin layers (few centimeters thick, i.e., less than 1% of the cavity
 497 height ($L_X = 5.3$ m)) near the horizontal walls in the one-cell regime. In the
 498 multiple-cell regime, the temperature variations are observed near the ceiling

499 for September and November, in a layer that extends over about 1 m with a
 500 maximum temperature located at a few tens of centimeters from the wall.

501 **5. Heat transfer analysis**

502 *5.1. Wall conductive fluxes*

503 In this subsection, we analyse the local heat transfer rates at the walls
 504 by quantifying the conductive wall heat flux q_{con} defined in Eq. (7). As the
 505 underlying physical mechanisms are very diverse, depending on the location
 506 on the wall or the month considered, we do not conduct this analysis in terms
 507 of dimensionless quantities; we aim to characterize the local heat transfer
 508 coefficient h in the Newton's law

$$q_{con} = h(T_{wall} - T_{gas}), \quad (12)$$

509 where T_{wall} is the local wall temperature and T_{gas} is the air temperature
 510 averaged over the entire domain.

511 In Fig. 11, q_{con} is plotted versus $T_{wall} - T_{gas}$ for the six months investi-
 512 gated and for each wall (each point corresponds to a given spatial location).
 513 Positive values correspond to heat transfer from the wall to the fluid. In
 514 the one-cell flow regime (left panels), we observe that the dependence of the
 515 conductive flux with $T_{wall} - T_{gas}$ is roughly linear. For a given month, a linear
 516 fit performed through the cloud of points (black line in the figures) allows to
 517 estimate empirically a single heat transfer coefficient h for all walls, ranging
 518 from $0.45 \text{ W.m}^{-2}.\text{K}^{-1}$ (in August) to $0.76 \text{ W.m}^{-2}.\text{K}^{-1}$ (in May), according
 519 to the magnitude of the convection flow. For the multiple cell regime (right
 520 panels), the conductive flux follows the same trend, except at the upper wall.
 521 The linear fit associated to all the walls except the upper one provides values
 522 of h ranging from 0.33 to $0.68 \text{ W.m}^{-2}.\text{K}^{-1}$. At the upper wall, $q_{con} \neq 0$ when
 523 $T_{wall} - T_{gas} = 0$ which means that T_{gas} is not the relevant reference temper-
 524 ature for the surrounding air layer. The actual reference temperature T_{bulk}
 525 is such that $q_{cond} = 0$ for $T_{wall} = T_{bulk}$ in the Newton's law. It can be easily
 526 deduced from the graphs in Fig. 11 that the averaged gas temperature T_{gas}
 527 underestimates T_{bulk} by approximately 0.03 K in February, 0.1 K in Septem-
 528 ber, and 0.15 K in November. This is in line with the analysis presented in
 529 the previous section. Indeed, we have shown that the air layer near the ceil-
 530 ing is warmer than the core region at T_{gas} , which implies that the reference
 531 temperature must be adjusted upwards.

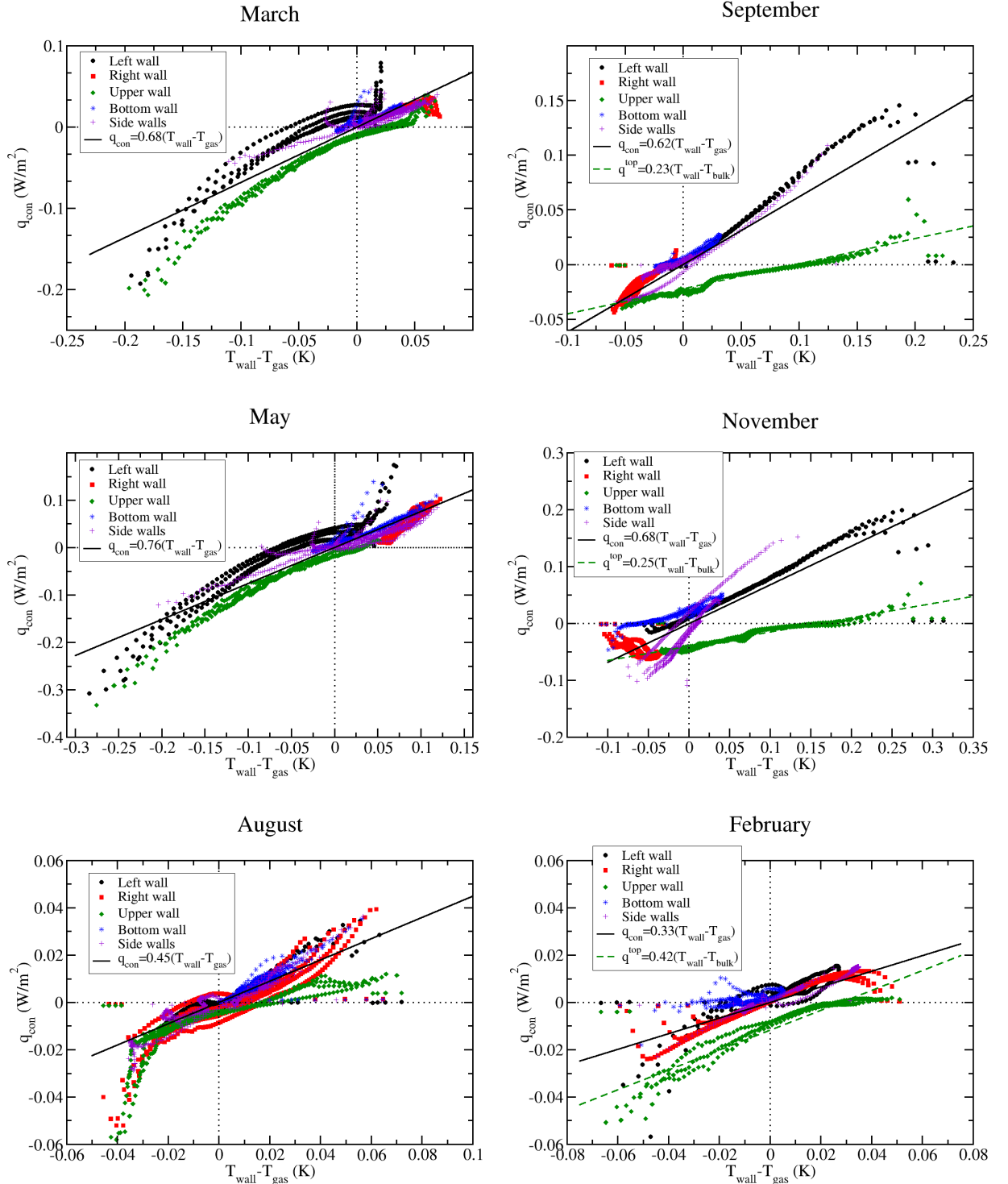


Figure 11: Cloud of points representing the local conductive heat flux at each wall versus the difference between the wall local temperature and the gas average temperature, for the six months investigated. Each point corresponds to a given spatial location on the wall. The black line represents the best linear fit of the cloud of points (with the exception of the top wall data in September, November and February). The green dashed line represents the best linear fit of the top wall in September, November and February, with T_{bulk} instead of T_{gas} .

532 By fitting both h^{top} and T_{bulk} , we get h^{top} ranging from $0.23 \text{ W}\cdot\text{m}^{-2}\cdot\text{K}^{-1}$
533 (in September) to $0.42 \text{ W}\cdot\text{m}^{-2}\cdot\text{K}^{-1}$ (in February). It is worthy to note that
534 all the values of the heat transfer coefficient h remain in a limited range,
535 from 0.23 to $0.76 \text{ W}\cdot\text{m}^{-2}\cdot\text{K}^{-1}$. This is not surprising given that the Nusselt
536 number usually scales as the Rayleigh number at the power 0.25 to 0.33
537 in natural convection [33], and thus increases slowly with the temperature
538 differences between the cavity walls. Therefore, these estimations of the heat
539 transfer coefficient might be used in a large-scale model coupling conduction
540 in the rock, radiative transfer in the cavity, and natural convection described
541 by the Newton's law (12). However, such approach raises the question of
542 how to define the reference gas temperature in the Newton's law. In the
543 case of complex non uniform temperature fields, relying on the averaged gas
544 temperature may result in large errors on wall convective heat fluxes.

545 5.2. Wall total fluxes

546 The aim of this section is to show the distribution of the conductive flux
547 q_{con} and to compare it to the distribution of the radiative flux q_{rad} and the
548 total heat flux $q_{tot} = q_{con} + q_{rad}$. We focus here on the months with the
549 highest conductive fluxes, i.e., May and November.

550 Fig. 12 presents the distribution of conductive (a and b), radiative (c and
551 d), and total (e and f) fluxes at the walls for the month of May. The radiative
552 flux largely dominates the conductive flux but the latter remains significant at
553 several spots, especially in the left ceiling region, downstream the left vertical
554 boundary layer and near the right bottom edge. The maximum total heat
555 flux in the system reaches in absolute value $1.15 \text{ W}/\text{m}^2$ and is concentrated
556 around the left upper edge. The conductive flux represents 40% of this value.

557 We show in Fig. 13 the distribution of q_{con} (a and b), q_{rad} (c and d),
558 and q_{tot} (e and f) for the month of November. It is worth noting that the
559 radiative flux distribution in November is opposite to that in May (tempera-
560 ture distributions are opposite), while this is not the case for the conductive
561 flux, sensitive to buoyancy. As in May, the system is mainly controlled by
562 radiative fluxes but there is still significant conductive heat flux in the upper
563 part of the left wall. Again, the maximum total heat flux reaches in absolute
564 value $1.15 \text{ W}/\text{m}^2$ and is concentrated at the left upper edge. The conductive
565 flux represents about 35% of the total flux in the upper part of the left and
566 side walls and in the majority of the right wall.

567 Heat transfer at the cavity walls is thus mainly dominated by the radiative
568 heat flux, with the exception of some localized spots where both conductive

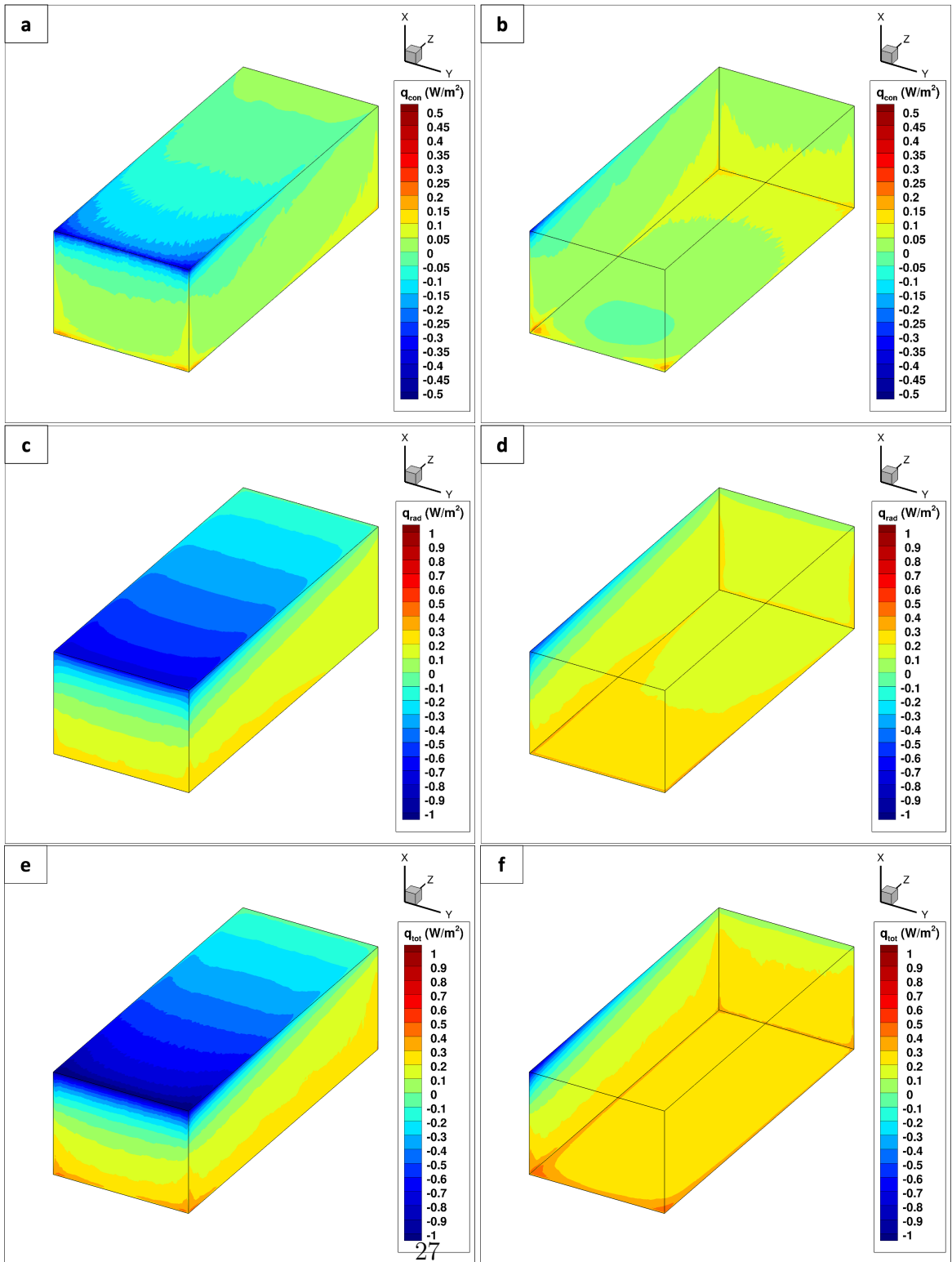


Figure 12: Spatial distribution of conductive (a and b), radiative (c and d) and total (e and f) heat fluxes at the walls for the month of May. The left part of the figure corresponds to the upper ($X = L_X$), left ($Z = 0$) and front ($Y = L_Y$) cave walls. The right part of the figure corresponds to the bottom ($X = 0$), right ($Z = L_Z$) and back ($Y = 0$) cave walls.

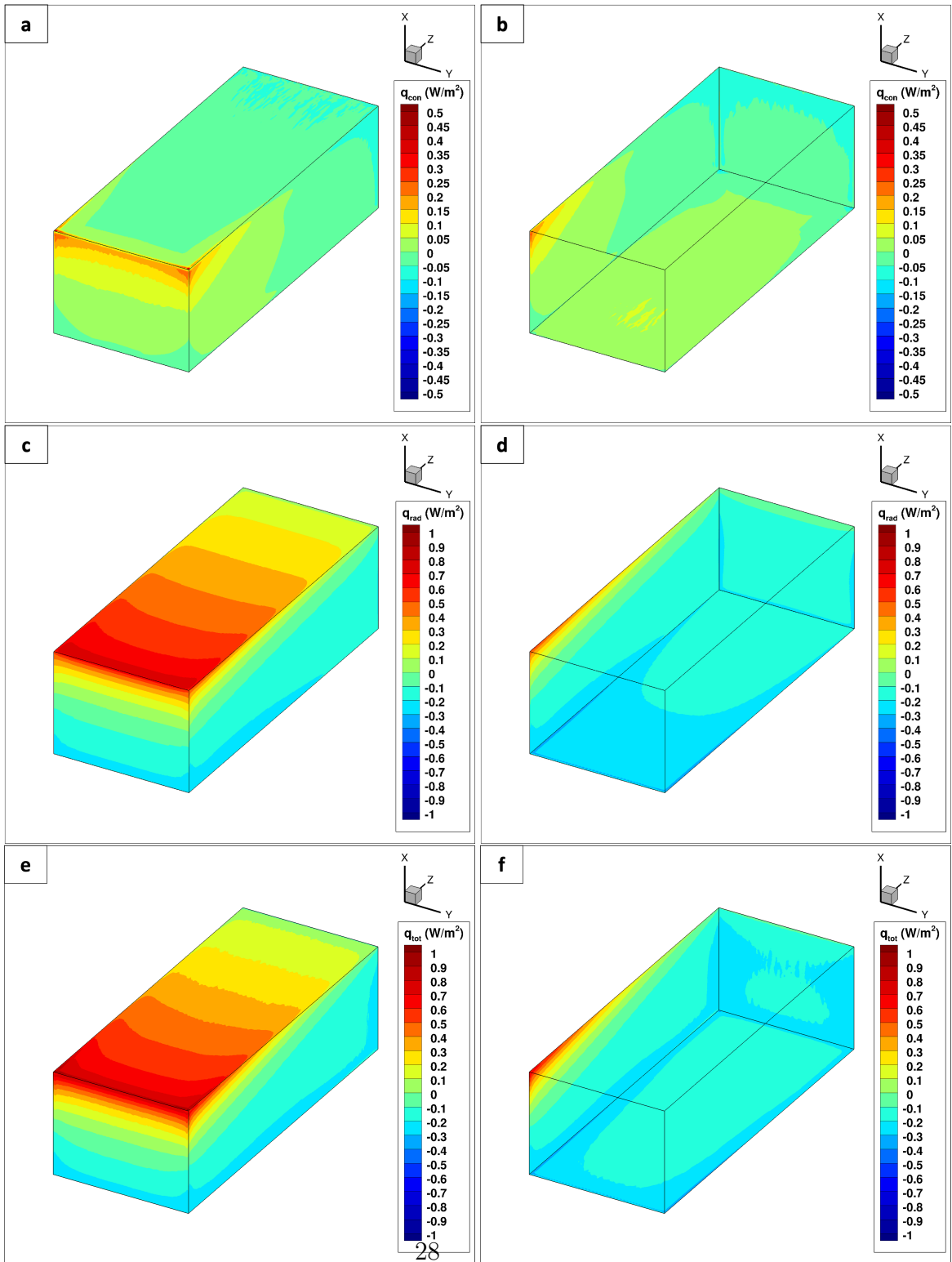


Figure 13: Spatial distribution of conductive (a and b), radiative (c and d) and total (e and f) heat fluxes at the walls for the month of November. The left part of the figure corresponds to the upper ($X = L_X$), left ($Z = 0$) and front ($Y = L_Y$) cave walls. The right part of the figure corresponds to the bottom ($X = 0$), right ($Z = L_Z$) and back ($Y = 0$) cave walls.

569 and radiative fluxes are on the same order. This conclusion must be tempered
570 by the fact that dry air was considered. In humid caves, convection controls
571 the heat flux associated with the latent heat of condensation and evaporation.
572 This probably affects the total heat flux. Assuming that solutal buoyancy
573 does not significantly modify the flow structure, the highest condensation
574 flux should occur in May and the highest evaporation flux in November, in
575 the region of the left upper edge in both cases. The effect of latent heat will
576 be investigated in a future work.

577 **6. Conclusion**

578 In this paper, the effect of turbulent natural convection on heat transfer
579 within a confined underground cavity was investigated using large eddy sim-
580 ulations based on the spectral vanishing viscosity method. Non-uniform wall
581 temperatures computed from a large-scale model and representative of exter-
582 nal climate condition at six times of the year were used as thermal boundary
583 conditions.

584 We identified two different flow regimes: (i) a one-cell flow regime asso-
585 ciated with strong convection and unstable mean vertical temperature gra-
586 dient, (ii) a multiple-cell flow regime associated with weak convection and
587 stable mean vertical temperature gradient. For each regime the mean direc-
588 tion of rotation of the flow is determined by the direction of the horizontal
589 temperature gradient. The one cell flow regime (March, May, August) is
590 characterized by a single-roll large-scale circulation, high turbulent fluctu-
591 ation level and strong mixing resulting in the homogenisation of the gas
592 temperature. The multiple-cell flow regime (September, November, Febru-
593 ary) is characterized by two counter-rotating large-scale structures. It corre-
594 sponds to a flow of weak intensity with low turbulent fluctuation level and a
595 significant vertical temperature gradient in the air near the ceiling.

596 The values of the heat transfer coefficient in the Newton's law were calcu-
597 lated from the LES results. We found that the flow intensity and turbulence
598 level have little influence on the heat transfer coefficient value. However, the
599 definition of the reference gas temperature to be used in the Newton's law
600 is a non trivial question in this problem with thermal boundary conditions
601 defined from complex temperature fields. The choice of the average gas tem-
602 perature is relevant when the air temperature is nearly uniform everywhere
603 in the core of the cavity. Otherwise, significant errors in the prediction of
604 wall heat fluxes may occur. This problem could likely be exacerbated by the

605 complex geometry of natural caves, making even more necessary the use of
606 CFD approaches as presented here.

607 Our method allows to determine if heat transfer at the cavity walls is
608 dominated by conducto-convective or radiative fluxes. Moreover, places in
609 the cavity and times of the year corresponding to intense heat transfer can be
610 identified. In future works, we will consider the coupling with mass transport
611 of water vapour in order to predict the conditions leading to intense conden-
612 sation, a problem of great importance for the conservation of painted caves.
613 In addition, given the significance of radiative fluxes, it might be worth in-
614 vestigating the effect of gas radiation associated with the presence of water
615 vapour and carbon dioxide in the cave atmosphere.

616 **Acknowledgements**

617 This work was funded by the financial support of the LabeX LaSIPS
618 (ANR-10-LABX-0032-LaSIPS) managed by the French National Research
619 Agency under the "Investissements d'avenir" program (ANR-11-IDEX-0003-
620 02). This work was granted access to the HPC resources of IDRIS under the
621 allocation 2020-A0062B00209 attributed by GENCI (Grand Equipement Na-
622 tional de Calcul Intensif). This work was also performed using HPC resources
623 from the "Mésocentre" computing center of CentraleSupélec and École Nor-
624 male Supérieure Paris-Saclay supported by CNRS and Région Île-de-France
625 (<http://mesocentre.centralesupelec.fr/>).

626 **References**

- 627 [1] D. Ford, P. Williams, Karst hydrogeology and geomorphology, John
628 Wiley & Sons, Ltd, 2007.
- 629 [2] I. J. Fairchild, A. Baker, Speleothem Science: From process to past
630 environments, John Wiley & Sons, Ltd, 2012.
- 631 [3] Y. Lv, Y. Jiang, W. Hu, M. Cao, Y. Mao, A review of the effects of tunnel
632 excavation on the hydrology, ecology, and environment in karst areas:
633 Current status, challenges, and perspectives, Journal of hydrogeology
634 586 (2020) 124891.
- 635 [4] D. C. Culver, T. Pipan, The Biology of caves and other subterranean
636 habitats, Oxford University Press, 2009.

- 637 [5] L. Quindos, A. Bonet, N. Diaz-Caneja, P. Fernandez, I. Gutierrez,
638 J. Solana, J. Soto, E. Villar, Study of the environmental variables affect-
639 ing the natural preservation of the Altamira Cave paintings located at
640 Santillana del Mar, Spain, *Atmospheric Environment* 21 (1987) 551–560.
- 641 [6] P. Malaurent, J. Brunet, D. Lacanette, J.-P. Caltagirone, Contribution
642 of numerical modelling of environmental parameters to the conservation
643 of prehistoric cave paintings: the example of Lascaux Cave, *Conserva-
644 tion and Management of Archaeological Sites* 8 (2006) 59–76.
- 645 [7] M. Luetscher, P.-Y. Jeannin, Temperature distribution in karst systems:
646 the role of air and water fluxes, *Terra Nova* 16 (2004) 344–350.
- 647 [8] M. Luetscher, B. Lismonde, P.-Y. Jeannin, Heat exchanges in the het-
648 erothermic zone of a karst system: Monlesi cave, Swiss Jura Mountains,
649 *J. Geophys. Res.* 113 (2008) F02025.
- 650 [9] J. Brunet, J. Vouvé, P. Malaurent, Re-establishing an underground cli-
651 mate appropriate for the conservation of the prehistoric paintings and
652 engravings at Lascaux, *Conservation and Management of Archaeological
653 Sites* 4 (2000) 33–45.
- 654 [10] F. Bourges, P. Genthon, D. Genty, M. Lorblanchet, E. Mauduit,
655 D. D’Hulst, Conservation of prehistoric caves and stability of their inner
656 climate: Lessons from Chauvet and other French caves, *Science of the
657 Total Environment* 58 (2019) 675–685.
- 658 [11] Y. Li, D. Ogura, S. Hokoi, J. Wang, T. Ishizaki, Behavior of an un-
659 derground stone chamber with 3-d modeling to restrain water-related
660 damage to mural paintings, *Journal of Asian Architecture and Building
661 Engineering* 13 (2014) 499–506.
- 662 [12] S. Sánchez-Moral, V. Soler, J. Cañaveras, E. Sanz-Rubio, R. Van
663 Grieken, K. Gysels, Inorganic deterioration affecting the Altamira Cave,
664 N Spain: quantitative approach to wall-corrosion (solutional etching)
665 processes induced by visitors, *Science of The Total Environment* 243-
666 244 (1999) 67–84.
- 667 [13] E. Villar, P. Fernandez, L. Quindos, J. Solana, J. Soto, Temperature of
668 rock surfaces in Altamira Cave (Spain), *Cave Science* 10 (1983) –.

- 669 [14] B. Guerrier, F. Doumenc, A. Roux, S. Mergui, P.-Y. Jeannin, Climatol-
670 ogy in shallow caves with negligible ventilation: heat and mass transfer,
671 *International Journal of Thermal Sciences* 146 (2019) 106066.
- 672 [15] N. Houillon, La dynamique du carbone inorganique dans le continuum
673 sol-épikarstique-cavité du site de la grotte de Lascaux (France), Ph.D.
674 thesis, University of Bordeaux (2016).
- 675 [16] J. Pallares, Laminar and turbulent Rayleigh-Bénard convection in a per-
676 fectly conducting cubical cavity, *International Journal of Heat and Fluid*
677 *Flow* 23 (2002) 346–358.
- 678 [17] L. Soucasse, Ph. Rivière, A. Soufiani, S. Xin, P. Le Quéré, Transitional
679 regimes of natural convection in a differentially heated cavity under the
680 effects of wall and molecular gas radiation, *Physics of Fluids* 26 (2014)
681 024105.
- 682 [18] J. Brunet, P. Malaurent, R. Lastennet, Évolution de l'état hydrique
683 d'une paroi de la Salle des Taureaux de la grotte de Lascaux :
684 conséquences pour la conservation, *Studies in conservation* 51 (2006)
685 241–251.
- 686 [19] W. Rohsenow, J. Hartnett, Y. Cho, *Handbook of heat transfer*, McGraw-
687 Hill (1998).
- 688 [20] D. Lacanette, S. Vincent, A. Sarthou, P. Malaurent, J.-P. Caltagirone,
689 An Eulerian/Lagrangian method for the numerical simulation of incom-
690 pressible convection flows interacting with complex obstacles: Applica-
691 tion to the natural convection in the Lascaux Cave, *International Jour-
692 nal of Heat and Mass Transfer* 52 (2009) 2528–2542.
- 693 [21] R. Pasquetti, Spectral vanishing viscosity method for LES: sensitivity
694 to the svv control parameters, *Journal of Turbulence* 6 (2005) 12.
- 695 [22] R. Siegel, J. Howell, *Thermal Radiation Heat Transfer*, Taylor & Francis,
696 2002.
- 697 [23] S. Xin, P. Le Quéré, An extended Chebyshev pseudo-spectral benchmark
698 for the 8:1 differentially heated cavity, *Numerical Methods in Fluids* 40
699 (2002) 981–998.

- 700 [24] S. Xin, J. Chergui, P. Le Quéré, 3D spectral parallel multi-domain com-
701 puting for natural convection flows, in: Springer (Ed.), *Parallel Compu-*
702 *tational Fluid Dynamics, Lecture Notes in Computational Science and*
703 *Engineering book series, Vol. 74, 2008, pp. 163–171.*
- 704 [25] P. Sagaut, *Large eddy simulation for incompressible flows*, Springer-
705 *Verlag (2006).*
- 706 [26] E. Tadmor, Convergence of spectral methods for nonlinear conservation
707 laws, *SIAM J. Numer. Anal.* 26 (1) (1989) 30–44.
- 708 [27] Y. Maday, S. Kaber, E. Tadmor, Legendre pseudo-spectral viscosity
709 method for nonlinear conservation laws, *SIAM J. Numer. Anal.* 30(2)
710 (1993) 321–342.
- 711 [28] G. S. Karamanos, G. E. Karniadakis, A spectral vanishing viscosity
712 method for large-eddy simulations, *Journal of Computational Physics*
713 163 (2000) 22–50.
- 714 [29] E. Severac, E. Serre, A spectral vanishing viscosity for the LES of tur-
715 bulent flows within rotating cavities, *Journal of Computational Physics*
716 226 (2007) 1234–1255.
- 717 [30] R. Pasquetti, Spectral vanishing viscosity method for large-eddy sim-
718 ulation of turbulent flows, *Journal of Scientific Computing* 27 (2006)
719 365–375.
- 720 [31] F. Wu-Shung, L. Yu-Chih, L. Chung-Gang, Estimation of turbulent nat-
721 ural convection in horizontal parallel plates by the Q criterion, *Int. Com.*
722 *Heat Mass Trans.* 45 (2013) 41–46.
- 723 [32] J. C. R. Hunt, A. A. Wray, P. Moin, Eddies, streams and convergence
724 zones in turbulent flows, In *Center for Turbulence Research, Proceedings*
725 *of the Summer Program (1988).*
- 726 [33] S. Grossmann, D. Lohse, Scaling in thermal convection: a unifying the-
727 ory, *Journal of Fluid Mechanics* 407 (2000) 27–56.